

Resolution of the MACHO-LMC-5 Puzzle: The Jerk-Parallax Microlens Degeneracy

Andrew Gould

*Department of Astronomy, The Ohio State University, 140 West 18th Avenue, Columbus,
OH 43210
gould@astronomy.ohio-state.edu*

ABSTRACT

By extending the constant-acceleration analysis of Smith, Mao, & Paczyński to include jerk, I show that microlens parallax measurements are subject to a four-fold discrete degeneracy. The new degeneracy is characterized by a projected velocity $\tilde{v}_j = -(3/4) \csc \beta_{\text{ec}} (\cos^2 \psi \sin^2 \beta_{\text{ec}} + \sin^2 \psi)^{3/2} v_{\oplus}$, where β_{ec} is the ecliptic latitude, ψ is the phase of the Earth’s orbit relative to opposition at the time of the event maximum, and $v_{\oplus} = 30 \text{ km s}^{-1}$ is the speed of the Earth. The degeneracy becomes important when the lens projected velocity \tilde{v} is of order \tilde{v}_j . For events toward the Large Magellanic Cloud, $\tilde{v}_j \simeq (3/4)v_{\oplus}$, so this degeneracy is important primarily for lenses in the Milky Way disk. In particular, it solves the puzzle of MACHO-LMC-5, whose microlens parallax measurement had yielded mass and distance determinations for the lens that were inconsistent with photometric estimates. Toward the Galactic bulge, \tilde{v}_j ranges from $\sim 0.2 \text{ km s}^{-1}$ at the solstice to $\sim 200 \text{ km s}^{-1}$ at the equinoxes, so the effect of the degeneracy depends strongly on the peak time of the event. The degeneracy applies mainly to events with Einstein timescales, $t_E \lesssim \text{yr}/2\pi$.

Subject headings: gravitational lensing — stars: low-mass

1. Introduction

The spectacular high-magnification microlensing event MACHO-LMC-5 has been a puzzle since its discovery was reported by the MACHO collaboration (Alcock et al. 1997). The “source star” for the event is quite red at baseline but lies well below the Large Magellanic Cloud (LMC) giant branch. On the other hand, the event itself is quite blue, indicating that the true lensed source is blue and that the red star at baseline is not being microlensed. Gould, Bahcall & Flynn (1997) proposed that the red star was a foreground M dwarf in the

Milky Way disk and that this M dwarf was in fact the microlens. While the optical depth of the Milky Way disk is extremely low, $\tau \sim 10^{-9}$, the MACHO survey was sufficiently big that one should expect of order one such event.

Hubble Space Telescope (HST) observations carried out by Alcock et al. (2000) and further analyzed by Alcock et al. (2001) virtually proved this conjecture. The *HST* Planetary Camera images taken 6.3 years after the event clearly show two stars, one blue and one red, separated by 134 mas. The chance that an unrelated foreground M dwarf would lie so close to a given microlensed source is only $\sim 10^{-4}$. Even the conditional probability of such an alignment, given that a red star was known to lie within the $\sim 2''$ MACHO PSF, is only a few percent. Alcock et al. (2001) therefore concluded that the red dwarf was in fact the lens.

However, this identification turned out to compound rather than resolve the puzzle of MACHO-LMC-5. The lightcurve of this event shows a clear asymmetry about its peak (see Fig. 1). Such asymmetries can be induced by parallax effects due to the Earth’s orbital motion (Gould 1992), as was first observed by Alcock et al. (1995) and subsequently in about a dozen other events. Measuring the parallax effect yields the (two-dimensional) velocity projected onto the observer plane, \tilde{v} , of the lens relative to the source. The lens mass and lens-source relative parallax are then given by,

$$M = \frac{\tilde{v}\mu_{\text{rel}}t_{\text{E}}^2}{4G}, \quad \pi_{\text{rel}} = \frac{\mu_{\text{rel}}}{\tilde{v}}, \quad (1)$$

where t_{E} is the Einstein crossing time (measured during the event), and $\mu = 134 \text{ mas}/6.3 \text{ yr} = 21.4 \pm 0.7 \text{ mas yr}^{-1}$ (measured from the *HST* image). Combining these various measurements, Alcock et al. (2001) found,

$$M = 0.036_{-0.004}^{+0.009} M_{\odot}, \quad \pi_{\text{rel}} = 5 \pm 1 \text{ mas}, \quad (\text{microlensing}), \quad (2)$$

the latter value being equivalent to a lens distance of $D_l \sim 200 \text{ pc}$.

Of course, the very fact that the lens could be seen would seem to argue against such a small, substellar mass. Indeed, from the observed color and magnitude of the lens, Alcock et al. (2001) estimated its mass and distance to be,

$$M = 0.11 \pm 0.02 M_{\odot}, \quad D_l = 650 \pm 190 \text{ pc} \quad (\text{photometric}). \quad (3)$$

One way out of this conflict would be simply to assume that the parallax measurement was wrong. With a measured timescale of $t_{\text{E}} \sim 30$ days, MACHO-LMC-5 was about a factor three shorter than any other event for which there is a reliable parallax. Moreover, the parallax detection was only at about the 5σ level, small enough that it could conceivably be the product of small and unrecognized systematic errors. However, Alcock et al. (2001) argued

that the parallax measurement could not be so easily dismissed because the direction of $\tilde{\mathbf{v}}$ derived from this measurement agreed with the measured direction of $\boldsymbol{\mu}_{\text{rel}}$ to within about 6° . The chance of such an agreement, if the parallax measurement were indeed spurious, is only about 3%. Thus, a decade after its discovery, the event remains truly a puzzle.

Here I show that the parallax solution for MACHO-LMC-5 is subject to a four-fold degeneracy. While two of these solutions are virtually identical to their counterparts, the other two lead to quite different estimates of the mass and distance. One pair of solutions is equivalent to the solution reported by Alcock et al. (2001). The other pair yields both a larger mass and larger distance. I show that these are consistent with the photometric determinations.

2. Microlens Parallax: The Geocentric Worldview

While it is customary to fit for microlens parallaxes in the frame of the Sun, it is actually possible to stay much closer to the data if one adopts the geocentric point of view, which is illustrated in Figure 2. This can be important, especially in cases like the present one in which the parallax is only weakly detected.

Let $\mathbf{s}(t)$ be the Earth-to-Sun vector in units of AU in the heliocentric frame. Let t_p be some fixed time, in practice a time very close to the time t_0 of the peak of the event as seen from the Earth, and evaluate the derivative of $\mathbf{s}(t)$ at this time,

$$\mathbf{v}_p = \left. \frac{d\mathbf{s}}{dt} \right|_{t_p}. \quad (4)$$

Then in the geocentric frame (and relative to its position at t_p), the Sun has a positional offset (see inset to Fig. 2),

$$\Delta\mathbf{s}(t) = \mathbf{s}(t) - (t - t_p)\mathbf{v}_p - \mathbf{s}(t_p). \quad (5)$$

Consider now observations toward an event at some given celestial coordinates, and define $\hat{\mathbf{n}}$ and $\hat{\mathbf{e}}$ as the unit vectors pointing north and east. The projected position of the Sun in the adopted frame will then be

$$(s_n, s_e) = (\Delta\mathbf{s} \cdot \hat{\mathbf{n}}, \Delta\mathbf{s} \cdot \hat{\mathbf{e}}). \quad (6)$$

Note that this coordinate system is right-handed.

Let (τ, β) be the position of the lens relative to the source in units of the Einstein ring. Explicitly,

$$\tau(t) = \frac{t - t_0}{t_E} + \delta\tau, \quad \beta(t) = u_0 + \delta\beta, \quad (7)$$

where

$$(\delta\tau, \delta\beta) = \pi_E \Delta \mathbf{s} = (\boldsymbol{\pi}_E \cdot \Delta \mathbf{s}, \boldsymbol{\pi}_E \times \Delta \mathbf{s}), \quad (8)$$

t_E is the Einstein crossing time, and u_0 is the lens-source separation at t_0 . More explicitly, $(\delta\tau, \delta\beta) = [s_n(t)\pi_{E,N} + s_e(t)\pi_{E,E}, -s_n(t)\pi_{E,E} + s_e(t)\pi_{E,N}]$. I define (τ, β) to be also right-handed, so that if $u_0 > 0$ then the lens is passing the source on its right as seen from the Earth. These equations serve to define the “vector microlens parallax” $\boldsymbol{\pi}_E = (\pi_{E,N}, \pi_{E,E})$, whose magnitude $\pi_E = |\boldsymbol{\pi}_E|$ gives the projected size of the Einstein ring, $\tilde{r}_E = \text{AU}/\pi_E$, and whose direction gives the direction of the lens relative to the source as seen in the adopted frame. That is, at $t = t_p$, $d(\tau, \beta)/dt = (1, 0)/t_E$. So if the lens is going due north [$\boldsymbol{\pi}_E = (\pi_{E,N}, 0)$], the parallax deviation $(\delta\tau, \delta\beta) = (s_n, s_e)\pi_E$, while if it is going due east, $(\delta\tau, \delta\beta) = (s_e, -s_n)\pi_E$, which, since both (τ, β) and (s_n, s_e) are right-handed, are the proper behaviors.

There are several advantages to using these variables. Most significantly, when the event is fit including the parallax effect, the parameters t_0 , u_0 , and t_E , will come out to be very similar to their values when it is fit without parallax. That is, these parameters are given directly by the data and do not depend on the parallax model. This can be very important for cases in which the parallax is not strongly constrained. In such cases, the trajectory relative to the Sun will also not be well constrained, so the errors in t_0 , u_0 , and t_E in the heliocentric frame will be huge. But these errors will also be extremely correlated, since whatever values one adopts, they must conspire to produce exactly the right peak amplitude at exactly the right time, and passing at exactly the right rate as seen from the Earth. The downside is that at the end of the day, one must still convert to heliocentric coordinates in order to extract some of the parameters. However, it is actually better to perform this step separately so as to be able to understand the various sources of uncertainty in the final measurement.

Also, note that I am fitting for $\boldsymbol{\pi}_E$ rather than $\tilde{r}_E \equiv \text{AU}/\pi_E$ or $\tilde{\mathbf{v}} \equiv (\tilde{r}_E/\tilde{t}_E)(\boldsymbol{\pi}_E/\pi_E)$. As with trigonometric parallaxes, microlens parallaxes are much better behaved than their inverse quantities, particularly when they are near zero. See also Gould (2000).

3. Parallax Fits

I begin with the data set obtained from the MACHO web site (<http://www.macho.mcmaster.ca>). The event has a total of 265 points in R_M and 352 in B_M . I eliminate 3 outliers (all at baseline) and find that the remaining points have a $\chi^2/\text{dof} = 0.65$ in each filter separately. This indicates that the errors have been overestimated. In principle, one might under these circumstances renormalize the errors by a factor $\sqrt{0.65} = 0.81$. However, the great majority

of the points are at baseline where the event is extremely faint, whereas most of the information of immediate interest comes from the highly magnified portions of the event, where the error corrections are not likely to be the same as for the baseline points. Hence I do not renormalize. As mentioned in the Introduction, the fit to a standard Paczyński (1986) curve, with 7 parameters, t_0 , u_0 , t_E , $f_{s,R}$, $f_{b,R}$, $f_{s,B}$, and $f_{b,B}$,

$$f_i(t) = f_{s,i}A(u[t]) + f_{b,i}, \quad A(u) = \frac{u^2 + 2}{u\sqrt{u^2 + 4}}, \quad (9)$$

where $[u(t)]^2 = u_0^2 + (t - t_0)^2/t_E^2$, shows clear asymmetric residuals. See Figure 1.

I then add two additional parameters, $\pi_{E,N}$ and $\pi_{E,E}$, which enter $[u(t)]^2 = [\tau(t)]^2 + [\beta(t)]^2$ through equations (7) and (8). At first, I use the no-parallax solution as my seed. The code converges to a solution that is inconsistent with the results of Alcock et al. (2001). See Table 1. I therefore explore a densely sampled grid over the rectangle $-2 \leq \pi_{E,N} \leq 6$, $-2 \leq \pi_{E,E} \leq 4$. The likelihood contours of this search are shown in Figure 3.

Figure 3 has a number of notable features. First, of course, it has two solutions. The second solution (to the northwest) is the same as the one found by Alcock et al. (2001). As shown in Table 1, the two solutions differ in χ^2 by less than 0.1. Hence, they are truly degenerate. Second, the high χ^2 contours to the southwest of the two solutions tend toward continuous straight lines with a position angle of about 149° (North through East). This is almost exactly perpendicular to the acceleration of the Earth (projected onto the plane of the sky, which has an amplitude of $0.52 \text{ km s}^{-1} \text{ day}^{-1}$ and a position angle of $238.^\circ 3$). That is, these contours derive from the parallax asymmetry that is due to the acceleration of the Earth along the direction of lens motion and which is clearly visible in Figure 1. For events with weak parallax, one obtains only this one-dimensional information about the parallax (Gould, Miralda-Escudé & Bahcall 1994). Evidently, MACHO-LMC-5 is relatively close to this situation (as one would expect from its brevity), but Figure 3 shows that this event lies in a region of the $\boldsymbol{\pi}_E$ diagram that is *beyond* this continuous degeneracy.

4. Four-fold Degeneracy

In fact, there are not just two solutions, but four. The other two solutions are obtained from the first two by first substituting $u_0 \rightarrow -u_0$ and then making very slight adjustments to the other parameters. This degeneracy was discovered by Smith, Mao & Paczyński (2003). See Table 1.

4.1. Analytic Description

To understand the nature of this degeneracy, I extend the approach of Smith et al. (2003) by Taylor expanding \mathbf{u} , the vector position of the lens relative to the source in the Einstein ring,

$$\mathbf{u} = \mathbf{u}_0 + \boldsymbol{\omega}t + \pi_E \left(\frac{1}{2} \boldsymbol{\alpha}t^2 + \frac{1}{6} \mathbf{j}t^3 + \dots \right) \quad (10)$$

where \mathbf{u}_0 is the vector impact parameter, $\boldsymbol{\omega}$ is the vector inverse timescale (i.e., $\omega = t_E^{-1}$ with direction given by the lens-source relative motion), and $\boldsymbol{\alpha}$ and \mathbf{j} are the apparent acceleration and jerk of the Sun relative to the Earth, both divided by an AU. Note that $\boldsymbol{\omega}$, $\boldsymbol{\alpha}$, and \mathbf{j} are all evaluated at $t = 0$ and that all are two-dimensional vectors. I impose $\mathbf{u}_0 \cdot \boldsymbol{\omega} = 0$, which is equivalent to assuming that t_0 (the time of closest approach) can be directly determined from the lightcurve and so does not require an additional parameter. Squaring equation (10) yields,

$$u^2 = \sum_{i=0}^{\infty} C_i t^i, \quad (11)$$

where,

$$C_0 = u_0^2, \quad C_1 = 0, \quad C_2 = -\alpha u_0 \pi_{E,\perp} + t_E^{-2} \quad (12)$$

$$C_3 = \alpha \frac{\pi_{E,\parallel}}{t_E} + \frac{1}{4} \alpha^2 t_E u_0 \boldsymbol{\pi}_E \times \boldsymbol{\pi}_j, \quad (13)$$

$$C_4 = \frac{\alpha^2}{4} (\pi_E^2 + \boldsymbol{\pi}_j \cdot \boldsymbol{\pi}_E) + \frac{1}{12} \frac{\Omega_{\oplus}^2}{\alpha} u_0 \pi_{E,\perp}, \quad (14)$$

where I have introduced the “jerk parallax”,

$$\boldsymbol{\pi}_j \equiv \frac{4}{3} \frac{\mathbf{j}}{\alpha^2 t_E}, \quad (15)$$

and where the subscripts “ \parallel ” and “ \perp ” indicate components parallel and perpendicular to the acceleration $\boldsymbol{\alpha}$. Note that I have made use of the fact that the Earth’s orbit is basically circular to approximate the derivative of the jerk as $-\Omega_{\oplus}^2 \boldsymbol{\alpha}$, where $\Omega_{\oplus} = 2\pi \text{ yr}^{-1}$.

If one has found one set of parameters $(u_0, t_E, \boldsymbol{\pi}_E)$ that fit the light curve, then one can empirically determine the constants (C_0, C_2, C_3, C_4) . Any other parameter combination $(u'_0, t'_E, \boldsymbol{\pi}'_E)$ that reproduces these constants will then provide an equally good fit to the lightcurve (at least to fourth order in t). In principle, one could solve equations (12)-(14) numerically, but more physical insight can be gained by solving them algebraically in two relevant limits.

4.2. The Constant-Acceleration Degeneracy

If we ignore the jerk and jerk-derivative terms, then equations (13) and (14) become,

$$C_3 = \alpha \frac{\pi_{E,\parallel}}{t_E}, \quad C_4 = \frac{\alpha^2}{4} \pi_E^2. \quad (16)$$

Smith et al. (2003) showed that equations (12) and (16) have two degenerate solutions, which are roots of the cubic equation,

$$x^3 - 2C_2x^2 + [C_2^2 - (\alpha u_0 \pi_E)^2]x + C_3^2 u_0^2 = 0, \quad (17)$$

where $x = t_E^{-2}$, and where all the parameters are evaluated at one solution. While the roots of cubics are normally ungainly, in this case one of the roots is known from having found the solution to the event numerically. I label this solution with unprimed variables ($t_E, \boldsymbol{\pi}_E, u_0$) and label the second (so far unknown) solution with primed variables ($t'_E, \boldsymbol{\pi}'_E, u'_0$). Hence, by dividing the cubic by the known root, it can be reduced to a quadratic, which is easily solved. I find,

$$t'_E = \left[(1 - 2\epsilon_\perp) \frac{1 + \sqrt{1 + [2\epsilon_\parallel / (1 - 2\epsilon_\perp)]^2}}{2} \right]^{-1/2} t_E \sim (1 + \epsilon_\perp) t_E, \quad (18)$$

where $\boldsymbol{\epsilon} \equiv \alpha t_E^2 u_0 \boldsymbol{\pi}_E$. As shown by Smith et al. (2003), the other second-model parameters follow easily from this evaluation,

$$u'_0 = -u_0, \quad \pi'_E = \pi_E, \quad \pi'_{E,\parallel} = \frac{t'_E}{t_E} \pi_{E,\parallel}. \quad (19)$$

Note that the relations between the timescales for the two pairs of solutions shown in Table 1 are almost exactly as predicted by equation (18): from the $u_0 < 0$ solutions, one would predict the timescales of the $u_0 > 0$ solutions to be 32.2137 and 32.7270 days respectively. The actual timescales differ fractionally from these values by $< 10^{-4}$.

4.3. The New Jerk-Parallax Degeneracy

To elucidate the new degeneracy, I consider the limit $u_0 \rightarrow 0$. Equations (13) and (14) then become,

$$C_3 = \alpha \frac{\pi_{E,\parallel}}{t_E}, \quad C_4 = \frac{\alpha^2}{4} (\pi_E^2 + \boldsymbol{\pi}_E \cdot \boldsymbol{\pi}_j), \quad (20)$$

for which the solution is,

$$\pi'_{E,\parallel} = \pi_{E,\parallel}, \quad \pi'_{E,\perp} = -(\pi_{E,\perp} + \pi_{j,\perp}), \quad (21)$$

and $t'_E = t_E$.

Note that for the special case $\pi_{E,\perp} = -\pi_{j,\perp}/2$, equation (21) implies that $\boldsymbol{\pi}'_E = \boldsymbol{\pi}_E$. That is, there is no degeneracy.

4.4. Full Solution

It is now possible to solve for the adjustments to the other parameters to first order in u_0 . For example, from the full expression for C_2 in equation (12), one finds,

$$\Delta t_E \simeq -\frac{\alpha t_E^2}{2}(\pi_{E,\perp}\Delta u_0 + u_0\Delta\pi_{E,\perp})t_E. \quad (22)$$

Note that for the degeneracy originally identified by Smith et al. (2003), for which $\Delta u_0 = -2u_0$ and $\Delta\pi_{E,\perp} = 0$, this equation reduces to the first-order evaluation of equation (18). However, it also correctly predicts the timescale differences of all four degenerate solutions listed in Table 1. For example, the difference between the t_E 's of the two $u_0 > 0$ (or the two $u_0 < 0$) solutions is predicted to be $\Delta t_E = 0.0134t_E$, whereas the actual differences are $0.0114t_E$ and $0.0158t_E$, respectively.

4.5. Comparison with Zero-Parallax Solution

The fifth line of Table 1 shows the best fit with the parallax enforced to be zero. Most of the seven parameters differ from their counterparts in the four parallax solutions by amounts that are large compared to the internal scatter of these solutions. This seems to contradict the claim made in § 2 that the advantage of the “geocentric worldview” is that the fit parameters do not substantially change with and without parallax. In fact, for high-magnification events with faint sources (like MACHO-LMC-5), the parameters that are well constrained by the fits are not u_0 , t_E , and F_s , separately, but rather the parameter combinations $F_{\max} = F_s/u_0$, $t_{\text{eff}} = u_0 t_E$, and their product $F_{\max} t_{\text{eff}} = F_s t_E$. To test this, I show in the sixth line of Table 1, the best fit zero-parallax solution with $F_{s,R}$ constrained to the value of the first parallax solution. The parameters of this solution show much better agreement with those of the parallax solutions, while χ^2 is increased by less than unity (for one more degree of freedom). Hence, the geocentric worldview is confirmed.

5. Lens Mass and Distance

To compare the direction of motion of the parallax solution with that of the *HST* proper-motion measurement, $\theta_{HST} = 138.^\circ 4$ (which reflects the time-averaged motion of the Earth and so is basically heliocentric), the parallax measurement must be converted from geocentric to heliocentric coordinates. This requires two steps. First, the parallax must be converted to the geocentric projected velocity,

$$\tilde{\mathbf{v}} = \frac{\text{AU}}{t_E} \frac{\boldsymbol{\pi}_E}{\pi_E^2}. \quad (23)$$

Next, one must add the Earth’s instantaneous velocity at t_0 to obtain the heliocentric projected velocity,

$$\tilde{\mathbf{v}}_{\text{hel}} = \tilde{\mathbf{v}} + \mathbf{v}_{\oplus}(t_0). \quad (24)$$

Finally, since the projected Einstein radius, $\tilde{r}_E = \tilde{v}t_E$, is the same in both frames, the heliocentric Einstein crossing time is,

$$t_{E,\text{hel}} = \frac{\tilde{v}}{\tilde{v}_{\text{hel}}} t_E. \quad (25)$$

These steps are illustrated in Figure 4. Also shown in this figure is the direction $\boldsymbol{\mu}_{\text{rel}}$ as measured by *HST*. Note that both parallax solutions are reasonably aligned with this direction, although the new solution is about twice as far from it as the original Alcock et al. (2001) solution. See Table 1.

I now combine the *HST* proper motion with each of the two parallax solutions to produce likelihood contours in lens mass and distance. For simplicity, and because the *HST* angular measurement error ($1.^\circ 0$) is so much smaller than the difference between it and either parallax solution, I treat the *HST* $\boldsymbol{\mu}_{\text{rel}}$ as a constraint, i.e., as having zero error. For each lens trial distance $D_l \simeq \text{AU}\pi_{\text{rel}}^{-1}$, I derive a heliocentric projected velocity, $\tilde{\mathbf{v}}_{\text{hel}} = \text{AU}\boldsymbol{\mu}_{\text{rel}}\pi_{\text{rel}} \simeq D_l\boldsymbol{\mu}_{\text{rel}}$. I convert this to a geocentric projected velocity $\tilde{\mathbf{v}}$ by inverting equation (24). Next, for each lens mass M , I infer a microlens parallax,

$$\pi_E = \sqrt{\frac{\pi_{\text{rel}}}{\kappa M}}, \quad \kappa = \frac{4G}{c^2 \text{AU}} \sim 8.1 \frac{\text{mas}}{M_{\odot}}, \quad (26)$$

and determine the geocentric Einstein timescale by $t_E = \text{AU}(\pi_E\tilde{v})^{-1}$. Finally, I find the vector geocentric microlens parallax $\boldsymbol{\pi}_E$ by inverting equation (23). For each (M, D_l) pair, I then minimize χ^2 holding the parameters $(\boldsymbol{\pi}_E, t_E)$ fixed at the values thus calculated. Figure 5 shows the resulting likelihood contours for the two sets of solutions. Each set of contours is shown relative to its own local minimum, which are offset from the global minimum (without the proper-motion constraint) by $\Delta\chi^2 = 2.0$ and $\Delta\chi^2 = 3.8$ for the original and new solutions

respectively. Note that while both sets of contours extend up to the hydrogen-burning limit at the few σ level, the old solution does so by moving toward smaller distances, while the new solution does so by moving toward larger distances. The best estimate for the lens mass and distance derived by Alcock et al. (2001) from its *HST* color and magnitude is shown by a circle with error bars. This is reasonably consistent (at the 2.5σ level) with the new solution but not the old one.

The reason for the divergent behaviors toward higher mass of the two sets of contours can be understood from Figure 4. As the distance is increased, so is the heliocentric projected speed, $\tilde{v}_{\text{hel}} \simeq D_l \mu_{\text{rel}}$. From Figure 4, this increases the magnitude of \tilde{v} for the new solution, but decreases it for the old solution. Since the geocentric timescale t_E is basically fixed directly by the lightcurve and so is approximately the same for all solutions, the mass $M \propto \tilde{v}_{\text{hel}} \mu_{\text{rel}} t_E^2$ moves in tandem with the heliocentric projected speed. Hence, the mass is correlated with the distance for the new solution but anticorrelated for the old solution.

6. Discussion

6.1. Levels of Parallax Degeneracy

The Taylor expansion of the (squared) lens-source separation, equations (11)-(14), allows one to understand analytically the various levels of microlensing parallax degeneracy. If there is only enough information in the lightcurve to measure the first two terms (out to C_2), then there is no information at all about π_{\parallel} , while π_{\perp} is completely degenerate with the timescale t_E . Hence, nothing can be learned about the parallax, and it is usually assumed to vanish.

If the next (C_3) term can be measured (and if the second term in eq. [13] can be ignored) then this equation allows a determination of π_{\parallel} , but π_{\perp} remains indeterminate. This is the degeneracy identified by Gould et al. (1994). Taking account of the second term in equation (13) leaves a linear continuous (i.e., line-like) degeneracy in the $\boldsymbol{\pi}_E$ plane, but rotates this line by an angle,

$$\theta_{\pi} = \tan^{-1} \frac{\eta \pi_{j,\parallel}}{1 + \eta \pi_{j,\perp}}, \quad \eta \equiv \frac{1}{4} u_0 \alpha t_E^2. \quad (27)$$

Since typically $\eta \pi_j \ll 1$, this angle is also usually very small, but it can be significant in some cases (see § 6.2).

If C_4 can be measured, then the continuous degeneracy is broken, but it is replaced by a four-fold discrete degeneracy. In this case, all four solutions lie along the line of the continuous degeneracy described in the previous paragraph. The transition from the continuous to

the discrete degeneracy is itself continuous. If C_4 is measured, but with only modest significance, then the error ellipses for each of the four solution will be extremely elongated along the line of continuous degeneracy. In this case, the two solutions with $u_0 > 0$ may merge. Similarly for the two solutions with $u_0 < 0$. However, the $u_0 > 0$ and $u_0 < 0$ solutions cannot merge with each other unless u_0^2 is consistent with zero. To break the discrete degeneracy requires sensitivity to the higher order terms, which is typically obtained only in relatively long events.

6.2. Broad Implications

For which microlensing events is the jerk-parallax degeneracy likely to be important? To address this question, it is best to think in terms of the “inverse projected velocity”, Λ ,

$$\Lambda \equiv \frac{\tilde{\mathbf{v}}}{\tilde{v}^2} = \frac{t_E}{\text{AU}} \boldsymbol{\pi}_E. \quad (28)$$

(I choose “ Λ ” for this quantity because it looks like an inverted “ \mathbf{v} ”.) Since t_E is virtually the same for all solutions, Λ is basically just a linear rescaling of $\boldsymbol{\pi}_E$. Its usefulness derives from the fact that the projected velocity (and so its inverse) is related solely to the kinematics of the event and thus is independent of the mass. Expressed in terms of this quantity, equation (21) becomes

$$\Lambda'_{\parallel} = \Lambda_{\parallel}, \quad \Lambda'_{\perp} = -(\Lambda_{\perp} + \tilde{v}_j^{-1}), \quad (29)$$

where,

$$\tilde{v}_j \equiv \frac{3}{4} \frac{\alpha^3}{\boldsymbol{\alpha} \times \mathbf{j}} \text{AU}. \quad (30)$$

(Note that since $\boldsymbol{\alpha}$ and \mathbf{j} are 2-dimensional vectors, the denominator is a signed scalar. See also eq. [13].) If we approximate the Earth’s orbit as circular, then \tilde{v}_j may be evaluated,

$$\tilde{v}_j = -\frac{3}{4} \frac{(\cos^2 \psi \sin^2 \beta_{\text{ec}} + \sin^2 \psi)^{3/2}}{\sin \beta_{\text{ec}}} v_{\oplus}, \quad (31)$$

where β_{ec} is the ecliptic latitude of the event, ψ is the phase of the Earth’s orbit at t_0 relative to opposition, and $v_{\oplus} = 30 \text{ km s}^{-1}$ is the speed of the Earth.

Note first that for LMC events, $\tilde{v}_j \simeq (3/4)v_{\oplus}$. For the great majority of LMC events, those with lenses in the Galactic halo or the LMC itself, $\tilde{v} \gg v_{\oplus}$. Hence, $\tilde{v}_j^{-1} \gg \Lambda$, so it would seem at first sight that the degeneracy would be very important. In fact, for events with $\tilde{v} \gg v_{\oplus}$, parallax effects will not generally be detectable unless the event is quite long, $\Omega_{\oplus} t_E > 1$. Such long events would most likely not in fact be degenerate because

the corresponding high-parallax solution would have strong signatures at Taylor-expansion orders beyond t^4 . It is only the disk-lens events, such as MACHO-LMC-5, for which this degeneracy is likely to cause confusion.

For events seen toward the bulge, the situation depends very strongly on the time of year. For definiteness, consider events toward Baade’s Window, for which $\sin \beta_{\text{ec}} \sim -0.1$. At opposition (roughly the summer solstice), $\tilde{v}_j = 0.0075 v_{\oplus} \sim 0.2 \text{ km s}^{-1}$, which is much slower than the \tilde{v} of any plausible event. In this case, the reasoning just given for the majority of LMC events applies, so the degeneracy is not likely to be important.

At quadrature (roughly the equinoxes) $\tilde{v}_j = 7.5 v_{\oplus} \sim 225 \text{ km s}^{-1}$, which is comparable to typical \tilde{v} for lensing of bulge sources by disk lenses and is smaller by a factor of a few than typical \tilde{v} for bulge-bulge lensing. Hence, this degeneracy could have significant impact on the interpretation of events peaking near the equinoxes.

At intermediate times, v_j scales roughly as $v_j \sim 7.5 v_{\oplus} \sin^3 \psi$, so that, for example, at $\psi = \pm 60^\circ$, $v_j \sim 145 \text{ km s}^{-1}$, still large enough to cause significant confusion.

I thank the referee, Shude Mao, for suggesting the inclusion of Figure 2, which significantly clarifies the adopted geometry. This work was supported by grant AST 02-01266 from the NSF.

REFERENCES

- Alcock, C., et al. 1995, ApJ, 454, L125
Alcock, C., et al. 1997, ApJ, 486, 697
Alcock, C., et al. 2000, ApJ, 552, 582
Alcock, C., et al. 2001, Nature, 414, 617
Gould, A. 1992, ApJ, 392, 442
Gould, A. 2000, ApJ, 542, 785
Gould, A., Bahcall, J.N. & Flynn, C. 1997, ApJ, 482, 913
Gould, A., Miralda-Escudé, J., & Bahcall, J.N. 1994, ApJ, 423, L105
Paczynski, B. 1986, ApJ, 304, 1

Smith, M., Mao, S., & Paczyński, B., 2003, MNRAS, 339, 925

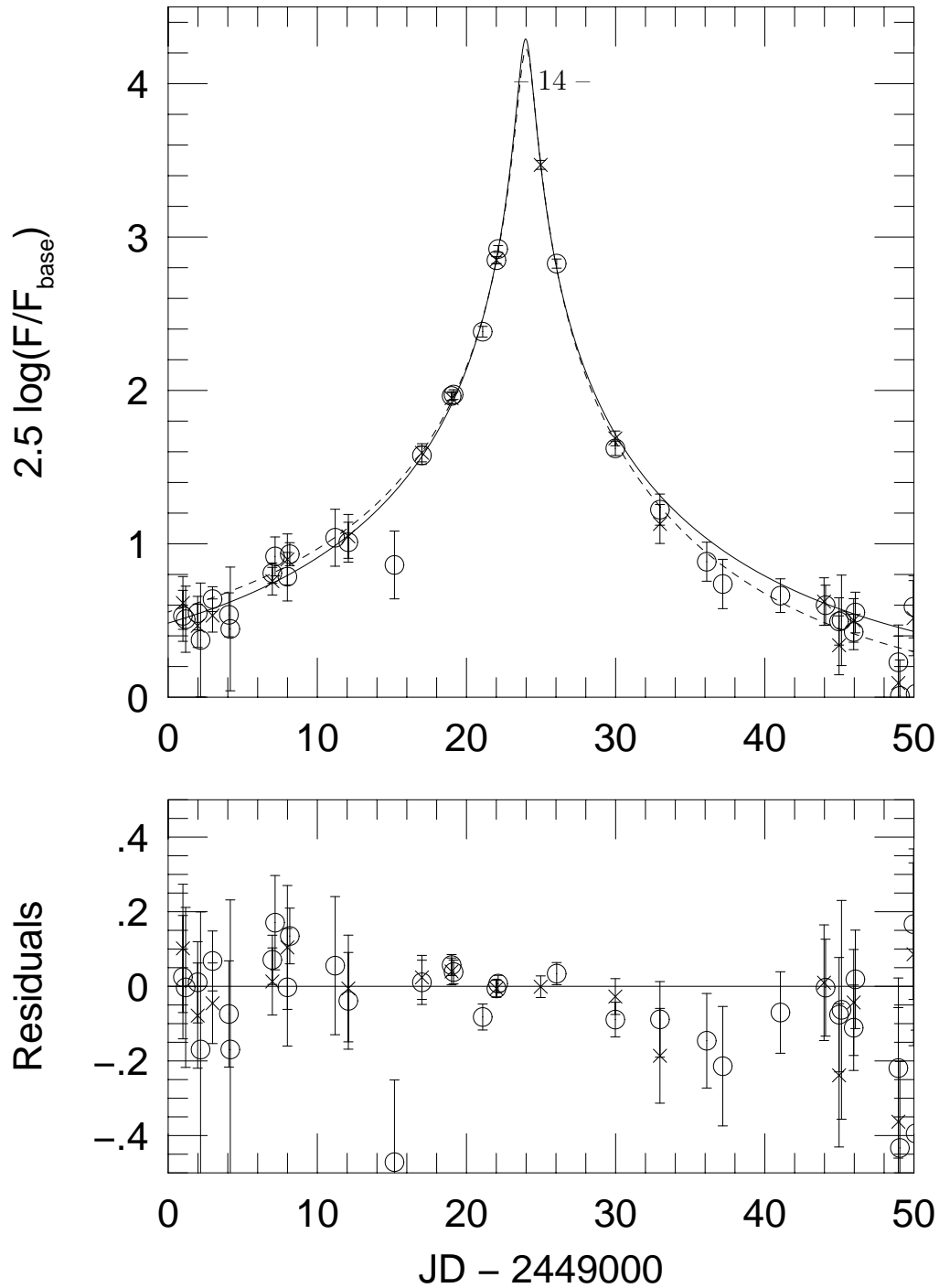


Fig. 1.— Lightcurve of MACHO-LMC-5 for MACHO red (*circles*) and blue (*crosses*) filters. Fluxes are normalized to $F_{\text{base}} \equiv F_s + F_b$ for red and are aligned to the same system via a linear transformation for blue. The solid curve is the best fit without parallax and shows clear asymmetric residuals, which are characteristic of parallax. See lower panel. The dashed curve shows the best fit with parallax.

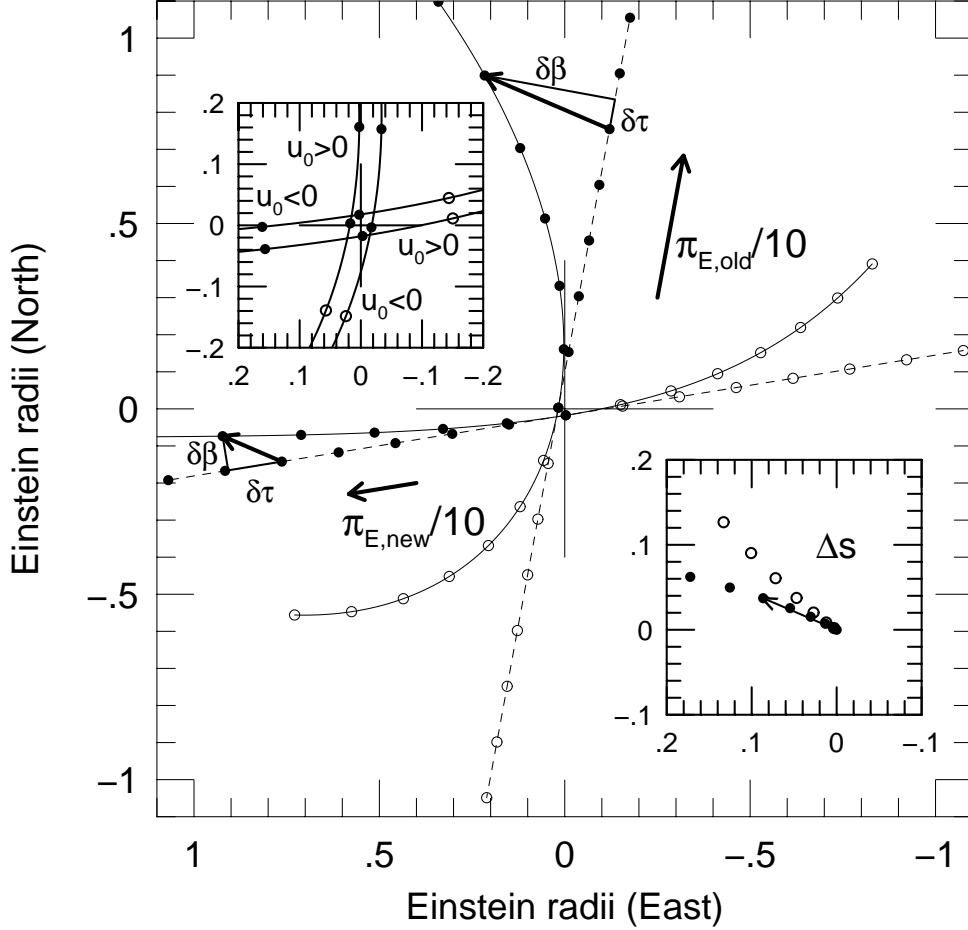


Fig. 2.— The geocentric view of microlens parallax for the old and new solutions of the event MACHO-LMC5, discussed in this paper. The inset at the lower right shows $\Delta\mathbf{s}(t)$, the apparent path of the Sun (in AU), relative to its position in the geocentric frame defined by the Earth’s motion at the peak of the event, and projected onto the plane of the sky in (east, north) coordinates. *Open circles* are for $t < t_0$ and *filled circles* are for $t \geq t_0$. Point separation is 5 days. The *dashed lines* represent the path of the lens relative to the source (*central cross*) in Einstein radii and in absence of parallax, with $(\tau, \beta) = ([t - t_0]/t_E, u_0)$. In both cases the lens passes the source on its right, so $u_0 > 0$. That is, the (τ, β) coordinate system is right-handed. The effect of parallax is to displace the lens by $(\delta\tau, \delta\beta) = \pi_E \Delta\mathbf{s} = (\pi_E \cdot \Delta\mathbf{s}, \pi_E \times \Delta\mathbf{s})$ to $(\tau, \beta) = ([t - t_0]/t_E + \delta\tau, u_0 + \delta\beta)$ (*solid curves*). The displacement vector is shown explicitly for $t = t_0 + 25$ days. Note that for both solutions, the offsets are parallel to $\Delta\mathbf{s}$ and their magnitudes are proportional to π_e . However, their decomposition into $\delta\tau$ and $\delta\beta$ is very different because the τ direction (the direction of motion and so also the direction of π_E) is different. The inset at the upper left displays all four degenerate solutions, including the two positive u_0 solutions shown in the main figure as well as the two negative u_0 solutions. See Table 1.

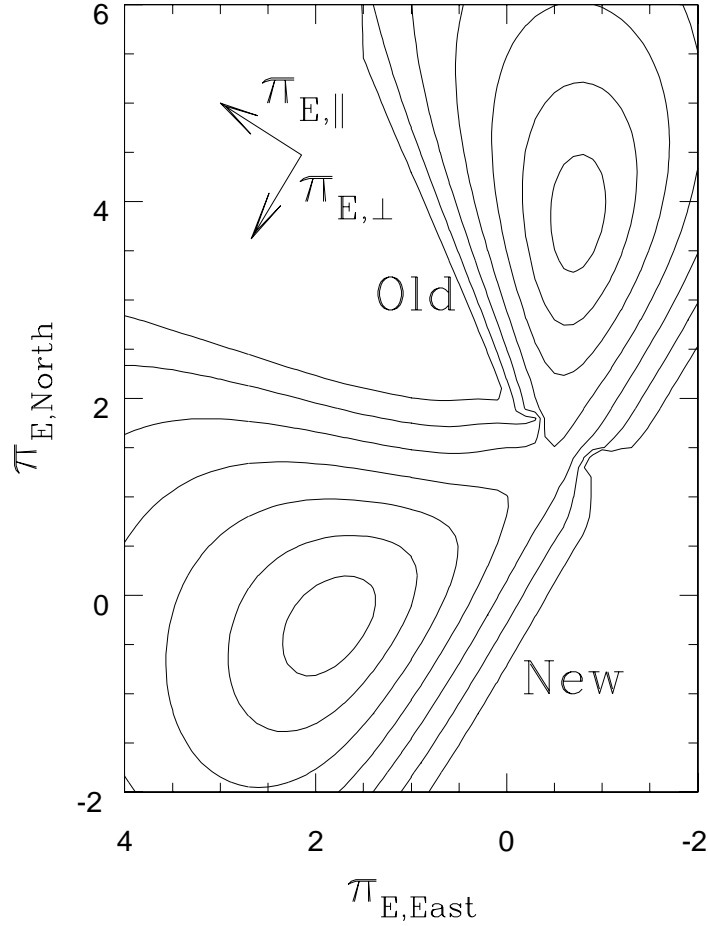


Fig. 3.— Likelihood contours in the π_E plane shown at $\Delta\chi^2 = 1, 4, 9, 16, 25, 36,$ and 49 relative to the minimum. There are two solutions, one to the northwest previously found by Alcock et al. (2001), and a new one to the southeast found in this paper. The directions of positive $\pi_{E,\parallel}$ and $\pi_{E,\perp}$ are shown as a “corner”. The offset between the two solutions is almost exactly aligned with the $\pi_{E,\perp}$ direction, which is perpendicular to the Earth’s acceleration vector at the event maximum. The diagram shows only the $u_0 < 0$ solutions, but the contours for $u_0 > 0$ are virtually identical. Note that π_E is dimensionless, since $\pi_E = AU/\tilde{r}_E$.

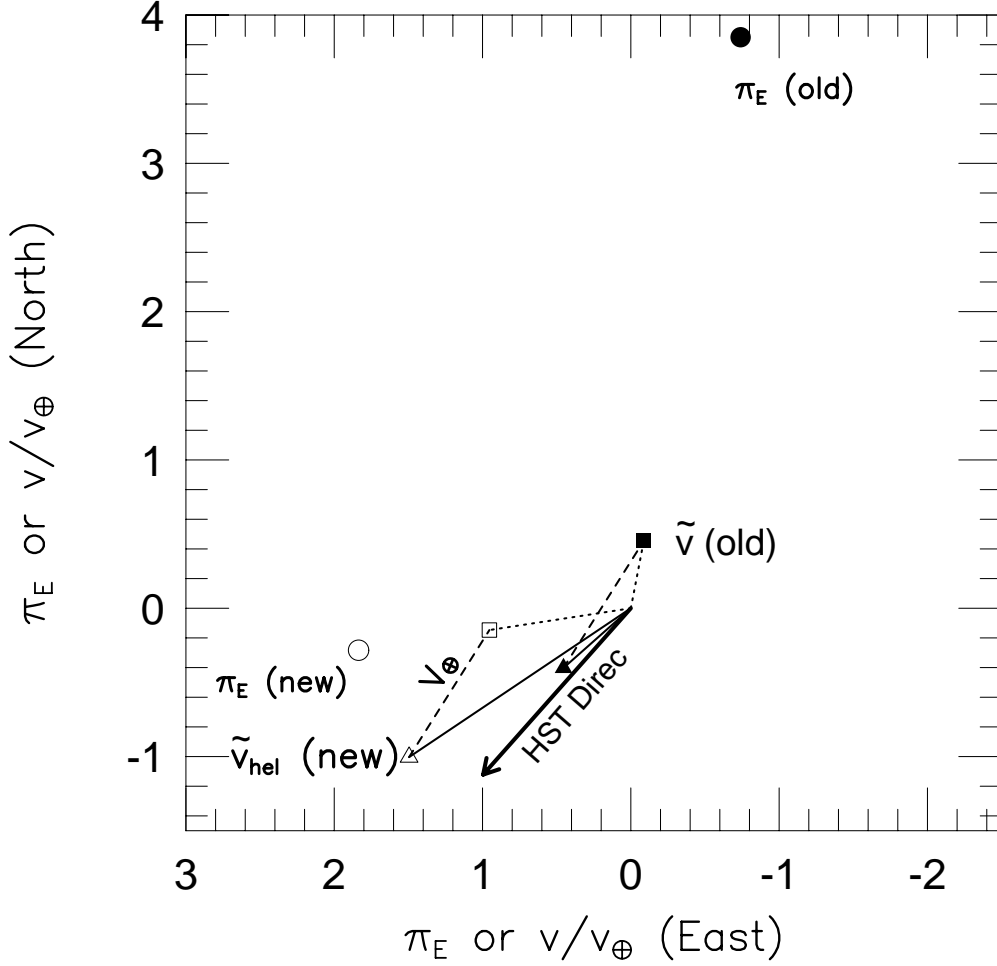


Fig. 4.— Transformation from directly observable to physically relevant quantities. Filled and open symbols are for the old (Alcock et al. 2001) and new (present paper) solutions, respectively. Geocentric vector parallaxes π_E (*circles*) are measured from the lightcurve together with standard microlensing parameters (see Fig. 3). Geocentric projected velocities \tilde{v} (*squares*) are found by inverting the magnitudes of π_E , but keeping the same directions. See eq. (23). The Earth velocity at event maximum (*dashed lines*) is added to each of these to obtain the heliocentric projected velocities \tilde{v}_{hel} . See eq. (24). The direction of these (*thin solid lines*) should be the same as that of the lens-source relative proper motion μ_{rel} measured by *HST*, which is shown as a bold line. Note that π_E is dimensionless, since $\pi_E = \text{AU}/\tilde{r}_E$.

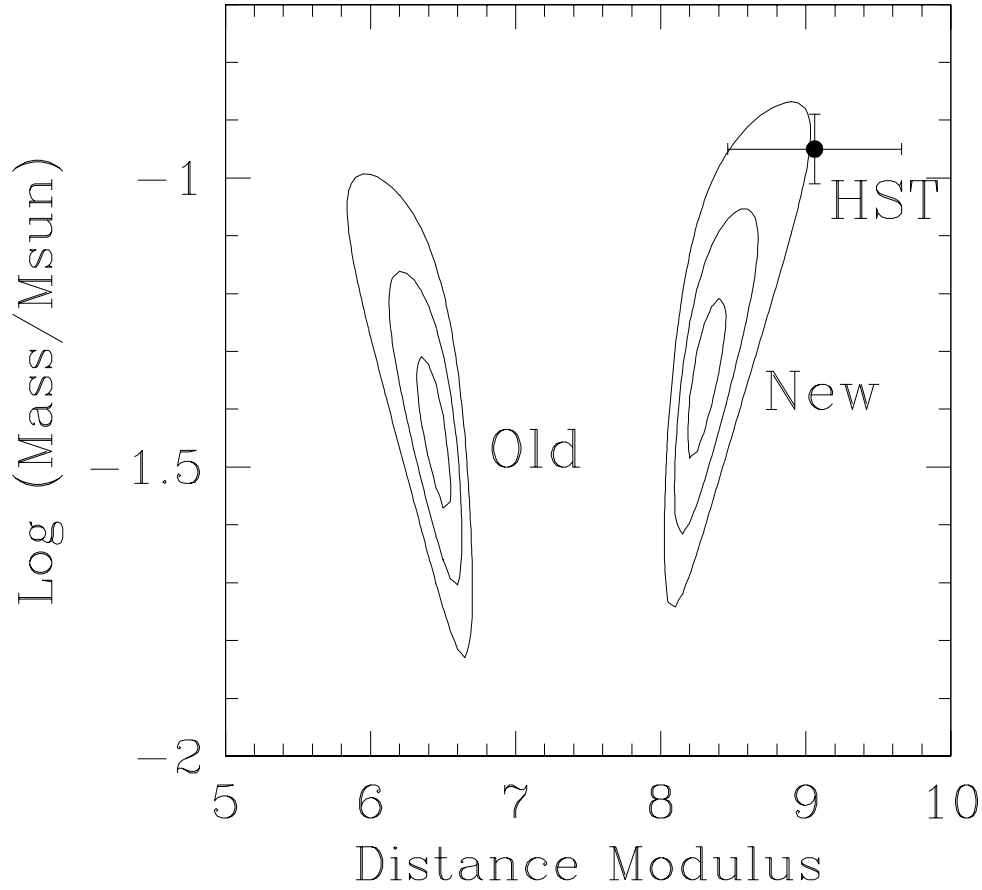


Fig. 5.— Likelihood contours ($\Delta\chi^2 = 1, 4,$ and 9) for lenses of mass M and distance modulus $5\log[D_l/10\text{ pc}]$, where D_l is the lens distance. The new solution lies to the right. The photometrically determined mass and distance (*filled circle*) are reasonably consistent with the new solution but are inconsistent with the old one.

Table 1. Four-fold Degenerate Solutions of MACHO-LMC-5

t_0 (days)	u_0	t_E (days)	$\pi_{E,N}$	$\pi_{E,E}$	$F_{s,R}$ (arb)	$F_{b,R}$ (units)	$F_{s,B}$ (arb)	$F_{b,B}$ (units)	\tilde{v}_{hel} (km s ⁻¹)	p.a. (deg)	χ^2
24.0010	-0.017651	32.4323	-0.2830	1.8358	29.8402	4.7585	29.2592	-13.5726	53.6223	123.88	395.5138
24.0005	0.017650	32.2161	-0.2969	1.8219	29.8384	4.7604	29.2574	-13.5708	54.0670	123.94	395.5146
24.0000	-0.017593	32.0641	3.8502	-0.7402	29.7723	4.8261	29.1934	-13.5071	18.0691	131.55	395.5762
24.0014	0.017590	32.7261	3.8279	-0.7036	29.7704	4.8280	29.1916	-13.5052	18.2789	131.62	395.5772
23.9653	0.015177	35.1955	0.0000	0.0000	27.2320	7.3797	26.6741	-11.3076			423.9113
23.9734	0.018172	32.7845	0.0000	0.0000	29.8402	4.8280	29.0951	-13.6066			424.5757